

Dual-Band Helical Edge States and Discrete Dirac Vortices in Solid-State Elastic Waves

Zi-Dong Zhang,¹ Si-Yuan Yu,^{1,2,*} Ming-Hui Lu,^{1,2,†} and Yan-Feng Chen^{1,2}

¹*National Laboratory of Solid State Microstructures & Department of Materials Science and Engineering, Nanjing University, Nanjing 210093, China*

²*Jiangsu Key Laboratory of Artificial Functional Materials, Nanjing University, Nanjing 210093, China*

(Received 24 January 2022; revised 17 February 2022; accepted 17 February 2022; published 10 March 2022)

Dual-band equipment has unique advantages as regards ensuring the stability of wireless communication and improving efficiency. With the development of topological photonics and phononics, electromagnetic and mechanical wave transmission with simultaneous advantages, e.g., antireflection, broadband, and nondispersion characteristics, has been simultaneously realized. This outcome has greatly improved elastic wave manipulation performance in solids, which are important media for wireless communication. Here, using a plate phononic crystal (PnC), a dual-mode elastic topological insulator is theoretically designed and experimentally realized, and the quantum spin Hall effect is observed under a dual band. Using discrete Kekulé modulation to construct the PnC multidomain junction, dual-mode and dual-band Dirac vortexes, i.e., a type of topological corner state, are obtained in a single PnC. These transmitted and localized topological states have the same excellent properties as their antecedents, which are obtained with single-band materials. The implementation mechanisms are diverse and applicable to multiple modes and broad frequencies, offering antijamming, low-loss, high-efficiency, and high-capacity signal processing components. The findings of this study will aid development of solid-state topology PnCs, as well as future topological-phononic integrated circuits with high performance and multifunctionality.

DOI: 10.1103/PhysRevApplied.17.034029

I. INTRODUCTION

In wireless communication, dual-band equipment can transmit signals in one of two standard frequency bands [1,2]. Compared with a single band, a dual band significantly improves the antijamming capability of equipment and adds additional bandwidth, thereby providing the greatest flexibility for wireless networking. For example, dual-band broadband routers that support 2.4- and 5-GHz channels have become the standard choice for home WiFi networks. On the other hand, elastic waves in solids are crucial information media for wireless communication [3,4]. Currently, most mobile terminals use surface or bulk acoustic waves (SAWs or BAWS, respectively) to filter radio-frequency signals. Compared with electromagnetic waves at the same frequency, elastic waves can have wavelengths that are five orders of magnitude shorter, thereby allowing a considerably smaller device footprint. Moreover, compared with fluid sounds, solid-state elastic waves have extremely low loss and mature on-chip transducing capabilities.

With the development of topological band theory for electromagnetics and mechanics [5–24], the ability to manipulate elastic waves in solids has increased to an unprecedented level. For example, by constructing phononic crystals (PnCs) with pseudospins, the quantum spin Hall effect (QSHE) can be simulated to realize “antireflection” transmission of one-dimensional (1D) elastic waves [10,12–15,18,20]. This finding has facilitated development of superior solid-state phononic waveguiding technology, which simultaneously possesses a high degree of freedom for routing, ultralow transmission loss, and immunity to various processing defects. In more depth, by introducing the concept of high-order topology, zero-dimensional (0D) localized corner states have been achieved, which facilitate high-quality mechanical resonators with small-mode volumes and multifunctional topological “cavity-waveguide” coupling systems [21–24]. Recently, topological dual-band 1D edge states have been confirmed experimentally in electromagnetic waves [25], airborne sounds [26,27], and even nanomechanical systems [28]. Topological multiband 0D corner states are also verified experimentally in airborne sounds [29], with predictions in electromagnetic systems [30–32]. Although the currently reported nanoelectromechanical work [28] concerns elastic waves, the complex structure

*yusiyuan@nju.edu.cn

†luminghui@nju.edu.cn

(i.e., patterned nanomembrane with acoustic impedance mismatch with the substrate) and low group velocities [33] makes it difficult to scale and integrate into mainstream microwave acoustic devices. Moreover, considerable air damping caused by the nanomembrane means that it needs to operate under a higher vacuum, further limiting its practical value. If similar functions can be achieved through a simple solid-state structure, it will be undoubtedly promising for monolithic topological phononic circuits working at scalable frequencies. However, modes in solid-state elastic systems are multiple with ubiquitous modal couplings. For example, three-dimensional (3D) solid-state volumes support both SAWs and BAWs, and quasi-two-dimensional (2D) thin plates support both shear horizontal (SH) modes and flexural modes [further subdivided into the antisymmetric (*A*) and symmetric (*S*) Lamb modes] [34,35]. This greatly increases the complexity and difficulty of dual-/multiband topological band engineering for elastic waves.

In this study, a dual-mode, dual-band elastic analogous QSHE is theoretically proposed and experimentally implemented. Based on a scalable plate PnC, we implement fundamental antisymmetric Lamb-mode (*A*0) and first-order antisymmetric Lamb-mode (*A*1) elastic pseudospins accompanied by quadruple Dirac cones at low (approximately 15 kHz) and high (approximately 65 kHz) frequency, respectively. Through Kekulé modulation, we realize a 1D topological edge state with “spin-momentum locking” features and a 0D Dirac vortex, all based on both the *A*0 and *A*1 modes at two separated frequency bands. The Dirac vortex design is simple and diverse due to this unique discretization modulation. This dual-band solid-state topological material has a total working bandwidth ($\Delta\omega/\omega_{\text{center}}$, where $\Delta\omega$ and ω_{center} are the working frequency domain interval and the corresponding center frequency, respectively) exceeding 20% (both the *A*0- and *A*1-mode bandwidths exceed 10%). In addition, the simple structure of the PnC allows easy expansion to a wider range of operating frequencies [e.g., at very-high frequency (vhf) and ultrahigh frequency (uhf)] and various piezoelectric substrates that are more suitable for micro-acoustic integration [e.g., lithium niobate, lithium tantalite, or aluminum nitride], providing a promising basis for future integrated, high-frequency, high-throughput, low-loss, antijamming phononic information materials and components.

II. DESIGN OF DUAL-MODE (*A*0 AND *A*1) SPIN-DEGENERATE PLATE PnCs

The proposed PnC is constructed on an aluminum alloy plate and is composed of Y-shaped opening slots arranged in a triangular lattice, as shown in Fig. 1(a). The PnC lattice constant is $a = 23$ mm, and the plate thickness is $d = 5$ mm. Figure 1(b) shows details of the unit cell, which contains

three different Y-shaped opening slots, marked *A*, *B*, and *C*, with each Y-shaped slot containing three identical arms labeled W_A , W_B , and W_C , respectively. All arms have the same length ($R = 12.5$ mm), but their widths can differ. Initially, $W_A = W_B = W_C = 6$ mm and the entire PnC has C_{3v} symmetry. Figures 1(c) and 1(d) show the Brillouin zone (BZ) and the calculated mechanical band structure, respectively. In the calculation, the plate density, Young’s modulus, and Poisson’s ratio are set to 2700 kg/m^3 , 70 GPa , and 0.33 , respectively. Two elastic Dirac cones with different frequencies appear at the *K* and/or *K'* points.

Because this PnC has mirror symmetry on the plate plane, its extensional and SH modes (both in-plane) are decoupled from its out-of-plane flexural modes. Hence, we can effectively distinguish these modes by defining a polarization index P_z , which indicates the out-of-plane displacement proportional to the total displacement of each mode:

$$P_z = \frac{\int_{V_u} |u_z|^2 dV}{\int_{V_u} (|u_x|^2 + |u_y|^2 + |u_z|^2) dV}, \quad (1)$$

where V is the unit-cell volume and u_x , u_y , and u_z are the polarizations of the displacements in the x , y , and z directions, respectively.

The P_z indexes of the in-plane extensional and SH modes are close to zero and those of the out-of-plane flexural modes are close to 1, as shown in Fig. 7. This study focuses on the flexural modes, which are colored black in the band structures and gray in the other modes.

The “zone folding” method is used to evolve the PnC [6]. In this manner, two quadruple Dirac degeneracies (i.e., four-fold Dirac cones) are folded at the Γ point at two different band-structure frequencies, as shown in Fig. 1(e). For the specific band folding process, see Fig. 8.

We conduct a series of numerical analyses to confirm the specific vibration modes of each mechanical band; the results are presented in Figs. 2(a)–2(h), which show the mechanical band evolution during the geometric transition from a flat plate to a plate PnC. As mentioned above, in our plate PnC, the in-plane and out-of-plane modes of the plate are decoupled. Hence, with gradual increases in the R and W values of the three arms in the Y-shaped slots, the five low-frequency bands are all pure antisymmetric breathing modes (i.e., the *A* modes), including the fundamental (i.e., *A*0) and first-order (i.e., *A*1) modes. Mode hybridization does not occur in the first five bands, but rather in the higher-frequency bands. For example, the sixth band corresponds to hybridization of the *A*0 and *A*1 modes.

From these analyses, we determine that the two Dirac cones appearing at the *K* points correspond to the *A*0 (at lower frequencies) and *A*1 (at higher frequencies)

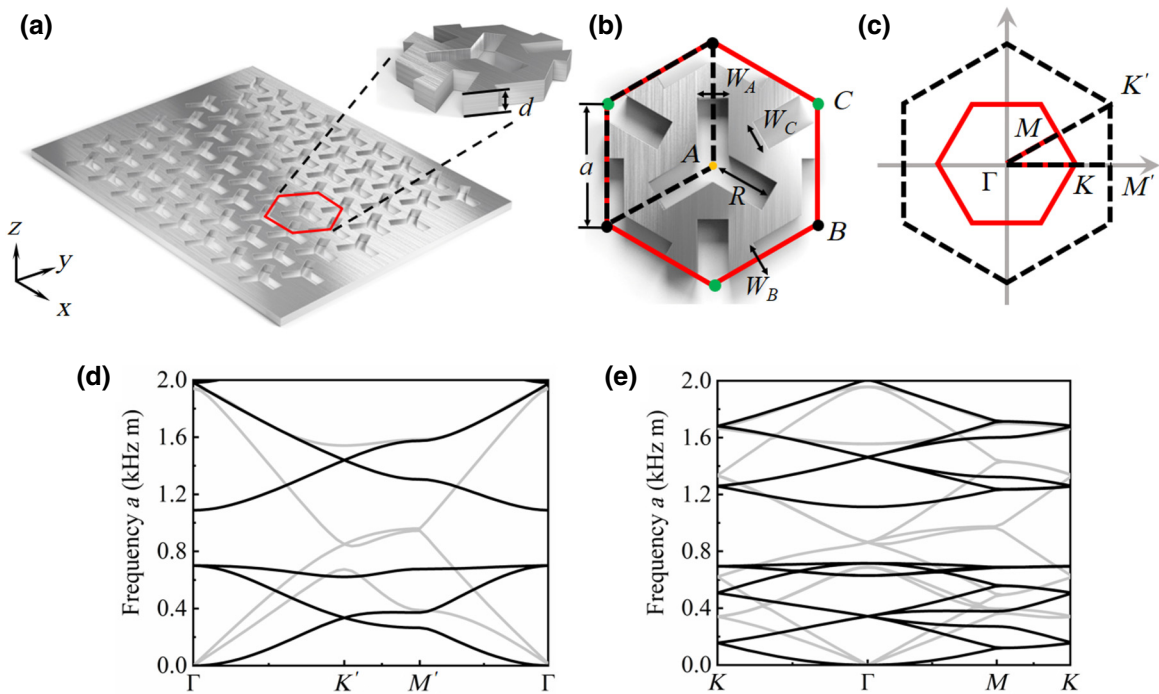


FIG. 1. Plate PnCs with dual-degenerate Dirac cones. (a) Schematic of PnC, which consists of Y-shaped slots in a triangular lattice; each slot has three arms. (b) Top view of enlarged unit cell. The plate thickness and lattice constant are represented by d and a , respectively. The crystal features three slot types, with identical R but (possibly) different arm widths W , i.e., W_A , W_B , and W_C . (c) BZ of triangular crystal. The black dotted line represents a primitive unit cell. (d) Calculated mechanical band structure of plate PnC when $W_A = W_B = W_C$. (e) Calculated band structure after “zone folding” (see Fig. 8 for details). For both band structures, two Dirac cones with different frequencies appear.

modes, respectively. That is, we successfully design a dual-mode ($A0$ and $A1$) spin-degenerate plate PnC. Figures 2(i) and 2(j) show the mechanical vibration distributions of

the $A0$ and $A1$ modes at the K points in the flat plate, respectively, and Figs. 2(k) and 2(l) show the distributions in the plate PnC, respectively. From the latter, the

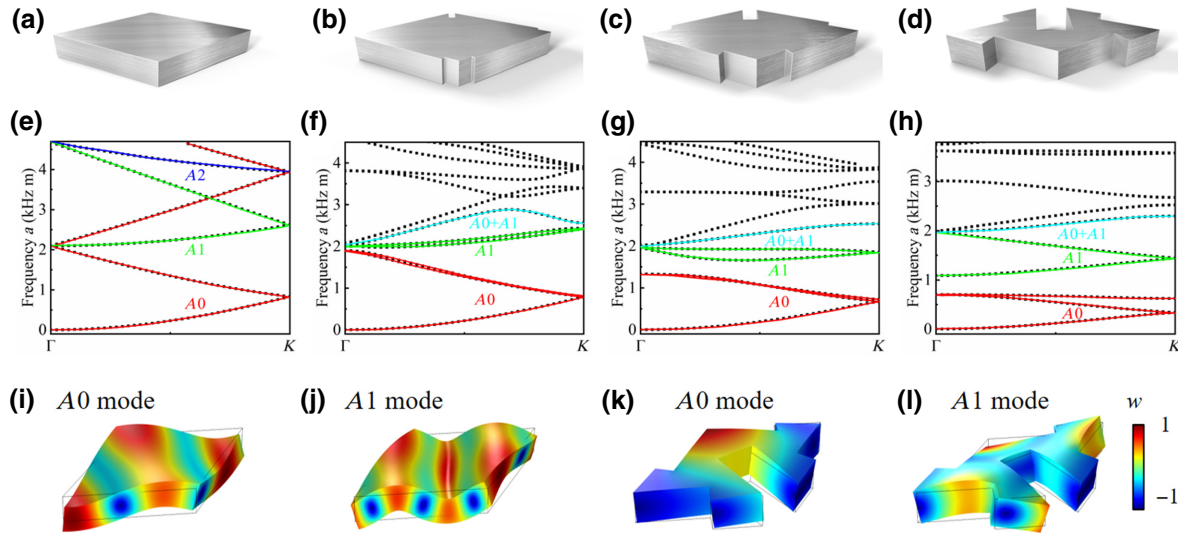


FIG. 2. Mechanical band structural evolution from flat plate to plate PnC. (a) Flat plate. PnCs with arm lengths and widths of (b) $R/4$ and $W/4$, respectively; (c) $R/2$ and $W/2$, respectively; and (d) R and W , respectively. (e)–(h) Band structures in Γ - K direction of flat plate and PnCs in (a)–(d), respectively. Mechanical vibrations of (i) $A0$ and (j) $A1$ modes for flat plate. Mechanical vibrations of (k) $A0$ and (l) $A1$ modes for final plate PnC. The colors indicate the amplitude of the out-of-plane displacement (w).

$A1$ modes have shorter Bloch wavelengths than the $A0$ modes.

III. BANDGAP OPENING VIA GENERALIZED KEKULÉ MODULATION

Next, we introduce Kekulé modulation to the PnC to break its spatial inversion symmetry and open the mechanical band gap [36–42]. Specifically, we set: $W_A = W + \delta W \cos \varphi$, $W_B = W + \delta W \cos(\varphi + 2\pi/3)$, and $W_C = W + \delta W \cos(\varphi + 4\pi/3)$, where the modulation strength $\delta W = 2.5$ mm. The R values remain unchanged. In most previous designs of topological photonic and phononic crystals (for example, through relaxation and contraction of the “hole-center distance” of a six-atom unit cell [13]), two discrete phases were constructed as $\varphi = 0$ and π . Compared with the previous discrete construction method, Kekulé modulation can generate a continuous vortex gap ranging from 0 to 2π , and can introduce new degrees of freedom (such as orbital degrees of freedom) to achieve innovative physical effects [40]. This modulation may also be used to realize a Dirac vortex and the topological effects of higher-dimensional space by introducing a new parameter space [36–42].

We calculate the mechanical bands of the proposed plate PnCs when $\varphi = 0$ and π , as shown in Figs. 3(a) and 3(b), respectively. Following breakage of the spatial inversion symmetry, the two four-fold Dirac degeneracies formed by the $A0$ and $A1$ modes both open, forming mechanical insulators in the two frequency bands. The $A0$ and $A1$ band gaps reach 15.87% and 12.24%, respectively. Comparison of the modes near the band gap (see their mechanical

distributions in Fig. 9) confirms that the two mechanical insulators (with $\varphi = 0$ and π) exhibit band inversion at both frequencies of the $A0$ and $A1$ modes. For simplicity, we refer to the PnCs with $\varphi = 0$ and π as “ordinary insulator” (OI) and “topological insulator” (TI), respectively, hereafter.

The effective Hamiltonian of the PnC is as follows [42]:

$$H(\mathbf{k}) = v_D \tau_0 \otimes (k_x \sigma_1 + k_y \sigma_2) + (m_1 \tau_1 - m_2 \tau_2) \otimes \sigma_3, \quad (2)$$

where k_i is the momentum, σ_i and τ_i are Pauli matrices, and v_D is the Fermi velocity. The two mass terms form a complex number $\mathbf{m} = m_1 + jm_2$, which can be estimated as $m \propto e^{i\varphi} \delta W$. Hence, the band gap can be adjusted by modulating phase φ and strength δW .

We next study the relationship between φ and the band gaps [see the results in Figs. 3(c) and 3(d)]. With changes in φ , both the $A0$ and $A1$ band gaps experience slight modulation of the $\pi/3$ angular periodicity, originating from the C_{3v} symmetry of the crystal. However, the extreme positions of the band gaps differ. In addition to φ modulation, adjustment of δW also affects the mechanical band, as shown in Fig. 10. As δW increases, both the $A0$ and $A1$ band gaps increase linearly.

IV. DUAL-BAND MECHANICAL HELICAL EDGE STATES OF $A0$ AND $A1$ MODES

Owing to the bulk-edge correspondence and topological band inversion described above, a pair of helical edge states exist on the boundary of two mechanical insulators $\varphi = \varphi_0$ and $\varphi = \varphi_0 + \pi$ [40]. We adopt $\varphi_0 = 0$ as an example to construct an interface composed of an OI ($\varphi = 0$) and TI ($\varphi = \pi$) adjacent to each other. Through supercell modeling, the mechanical band structures of the OI-TI interface are calculated; the results are shown in Fig. 4(a). In the bulk band gaps of the $A0$ and $A1$ modes, helical edge states appear. These edge states exhibit properties that are accompanied by pseudospins. Specifically, their mechanical vibration exhibits chirality formed by two independent modes, i.e., symmetric (Sym) and antisymmetric (Asym) modes, as $\text{Sym} \pm i\text{Asym}$ [6,8,13]. Figures 4(b) and 4(c) show the appearance of the symmetric and antisymmetric modes in the $A0$ and $A1$ bands, respectively. Clearly, the mechanical energy penetration from the OI-TI interface to the bulk (or “skin depth”) of the $A0$ mode significantly exceeds that of the $A1$ mode. Note that small band gaps exist in the centers of the edge states [13,15].

Helical edge states are known for their “spin-momentum locking” ability. Each of the two time-reversal dispersions corresponds to a spin or pseudospin. Without a “spin-reversal” mechanism, no guided mode of the helical edge states in one direction can be converted to its time-reversal counterpart in the opposite direction. In other

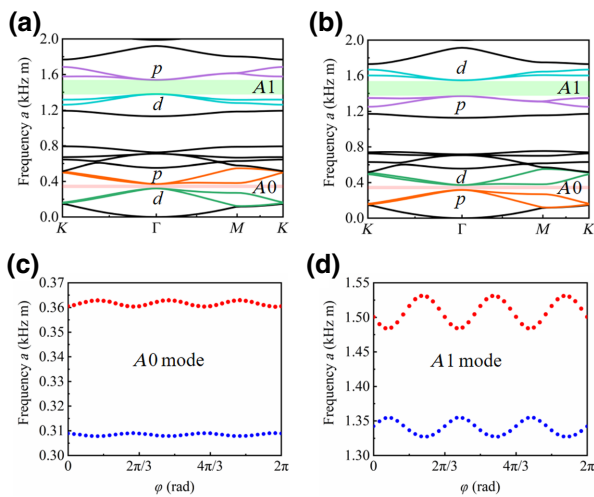


FIG. 3. Band-gap opening due to generalized Kekulé modulation. Mechanical band structures under applied homogeneous Kekulé modulation with (a) $\varphi = 0$ and (b) $\varphi = \pi$. The pink and green shaded regions correspond to the bulk band gaps of the $A0$ and $A1$ modes, respectively. (c) $A0$ and (d) $A1$ band gaps with variation of φ .

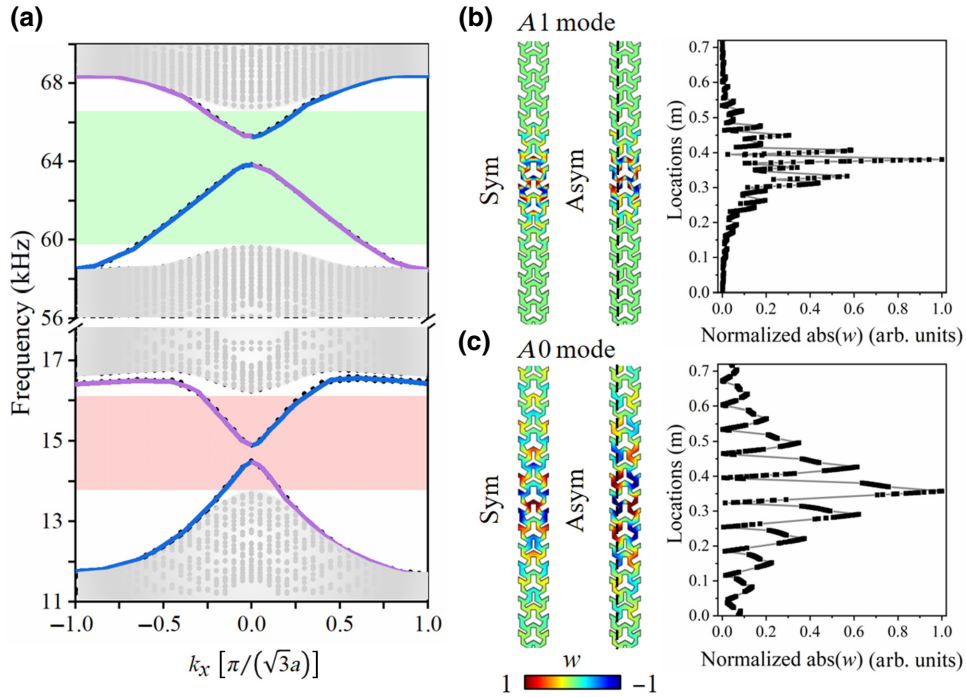


FIG. 4. Dual-mode/band topological protected helical edge modes. (a) Calculated band structures for A_0 and A_1 modes in interface between OI ($\varphi = 0$) and TI ($\varphi = \pi$). The blue and purple lines represent pseudospin+ and pseudospin-edge states hybridized from symmetric (Sym) and antisymmetric (Asym) modes. Representative examples of mechanical distributions for Sym and Asym modes from (b) A_1 and (c) A_0 bands at $k_x = 0$. The displacement field of a cross section of the plate (the corresponding position of the black dotted line) as a function of position is shown by line graph on the right-hand side of the figure, which can clearly display different “skin depth” for A_0 and A_1 Lamb waves.

words, the propagation of mechanical waves on the TI-OI interface in our system should be “reflection-free,” even in the presence of defects or bending, as none of these factors can cause spin reversal. Therefore, high transmission efficiency of mechanical energy should be obtained.

To experimentally verify this behavior, we fabricate a PnC sample containing a Z-type (two 120° bends) TI-OI interface, as shown in Fig. 5(a). We then measure the dual-port transmittance of this curved interface in the A_0 and A_1 frequency bands, as shown in Figs. 5(b) and 5(c), respectively. For details of our sample preparation and experimental measurements, see Sec. II. The bulk band-gap frequency measured in the experiment is slightly lower than our theory-based expectation, but the bandwidth is the same. The TI-OI interface transmission at the bulk band gap is considerably higher than that of the TI-OI interface itself. Using the spatial Fourier transform method [15], we also experimentally map the edge-state band structures, as shown in Fig. 11. The measurement results match the theory-based expectations.

Further, we numerically map mechanical wave propagation at the curved interface at frequencies of 14.5 kHz (A_0 mode) and 60 kHz (A_1 mode). The results are presented in Figs. 5(d) and 5(g), showing that mechanical waves at the interface smoothly traverse the bends. Moreover,

the transmission energy exhibits almost no drop on the interface, proving its antireflection characteristic. Through laser vibration measurements, we experimentally map the mechanical waves at the same frequencies. Figures 5(e) and 5(h) show these results, which again confirm that the mechanical waves successfully traverse the 120° bends. Comparison of the experimentally mapped edge states for the two frequencies reveals that the A_1 -mode mechanical energy localization is better on the TI-OI interface, i.e., the skin depth is relatively small. However, the A_1 modes exhibit more significant transmission loss than the A_0 modes. Finally, Figs. 5(f) and 5(i) show the experimentally measured mechanical energy intensity along the PnC incident and exit ends at the two frequencies, respectively. In the A_0 mode, the mechanical-wave intensity near the exit port is similar to that near the entrance port. However, in the A_1 mode, the intensity near the exit port decreases significantly. This may be due to the smaller Bloch wavelength of the A_1 mode; however, further exploration of this aspect is required.

Importantly, the simple structure of our proposed PnC endows it with high scalability. Through numerical simulation, similar dual-band functions on the vhf and uhf are demonstrated on a lithium niobate single-crystal plate with a thickness of 800 nm (see Appendix F).

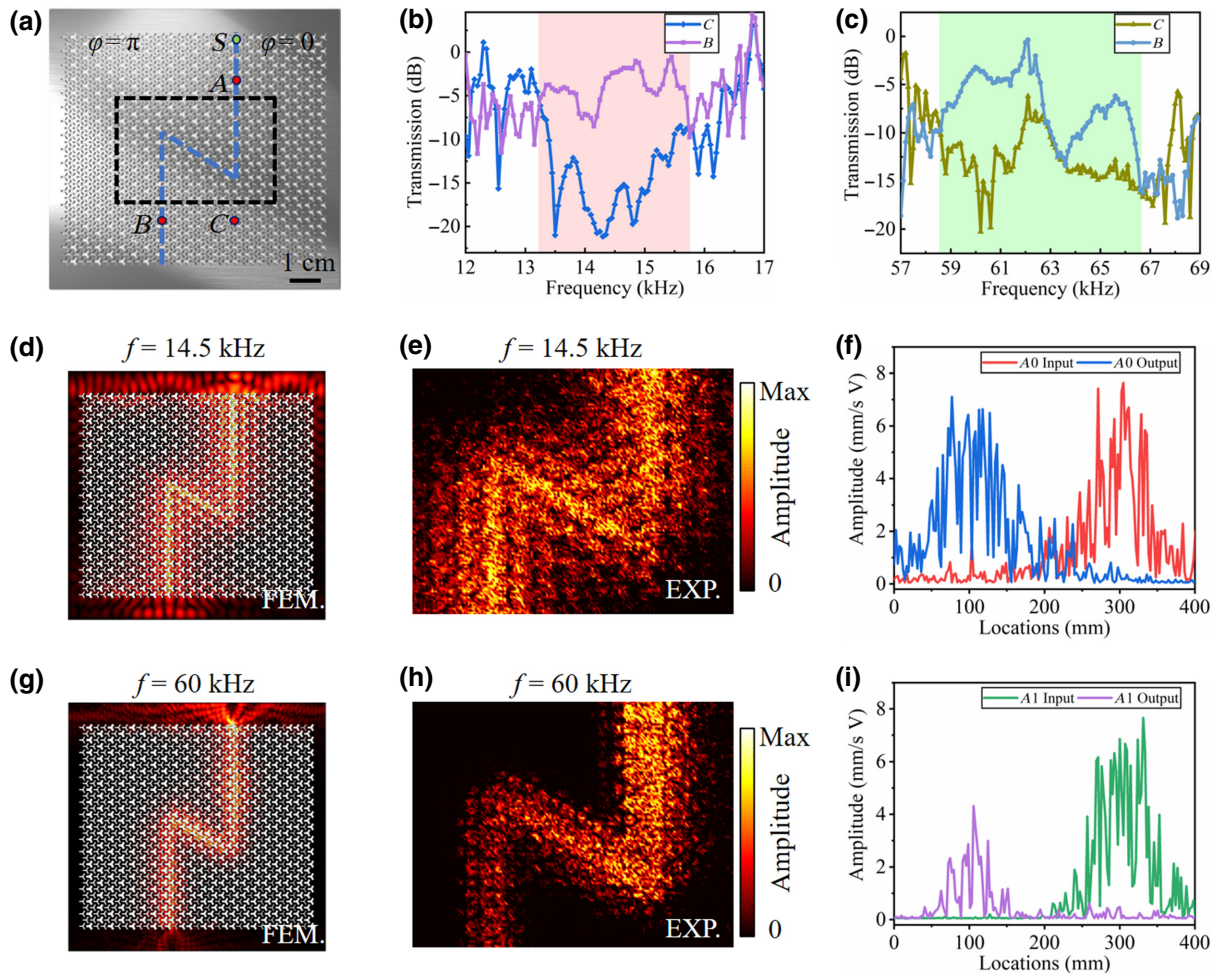


FIG. 5. A_0 and A_1 edge-state propagation along Z-type TI-OI interface. (a) Sample image: the blue dashed line marks the interface. A mechanical source is mounted at point S . Measured transmission spectra of mechanical waves near (b) A_0 and (c) A_1 bulk band gaps. Each spectrum shows the mechanical intensities measured at points B and C , compared with the value measured at point A . (d),(g) Simulated and (e),(h) measured mechanical displacement fields at curved interface, and (f),(i) measured mechanical energy intensities along PnC incident and exit ends, at 14.5 kHz (A_0 mode) and 60 kHz (A_1 mode), respectively.

V. 0D DISCRETE DIRAC VORTEX STATES OF MECHANICAL WAVES

An important research frontier is achievement of 0D Dirac vortex states using Kekulé modulation. Generally, topological corner states (TCSs) are realized based on the specific topological properties of two meeting edges running along different crystal directions; thus, the potential corner angles are limited (e.g., 90° for square lattices [43–46] and 60° for Kagome lattices [47,48]). Previously, through continuous Kekulé modulation, TCSs were realized in arbitrary polygonal domains [42]. However, continuous modulation is not necessary for realization of Dirac vortex states. Recently, a similar phenomenon was theoretically achieved through discrete phase modulation [41,49]. Although discrete modulation reduces the bandgaps of the (2D) bulk and (1D) edge modes, i.e., where the (0D) corner

states could exist, when the modulation phase is $2\pi/3$, this effect on the bandgap width is not obvious.

We conduct experiments on a sample with a corner, which has a domain angle of 120°, formed by discrete modulation, as shown in Fig. 6(a). For three crystal domains with $\varphi = 0$, $2\pi/3$, and $4\pi/3$, we obtain a single vortex with the simplest winding number, i.e., $n_w = 1$. These phase vortices guarantee the emergence of TCSs through the Jackiw-Rossi mechanism [37,38,50]. That is, the winding of $\varphi(\mathbf{r})$ is position dependent, and introduces phase vortices for the Dirac mass $m(\mathbf{r})$; these vortices are referred to as “Dirac vortices” [38]. Figure 6(b) shows the numerically evaluated eigenfrequencies for the A_0 and A_1 modes of our sample. Compared with continuous Kekulé modulation, discrete modulation introduces 1D interfaces to the system. The mechanical band structures of these interfaces are calculated and are shown in Fig. 14 (see

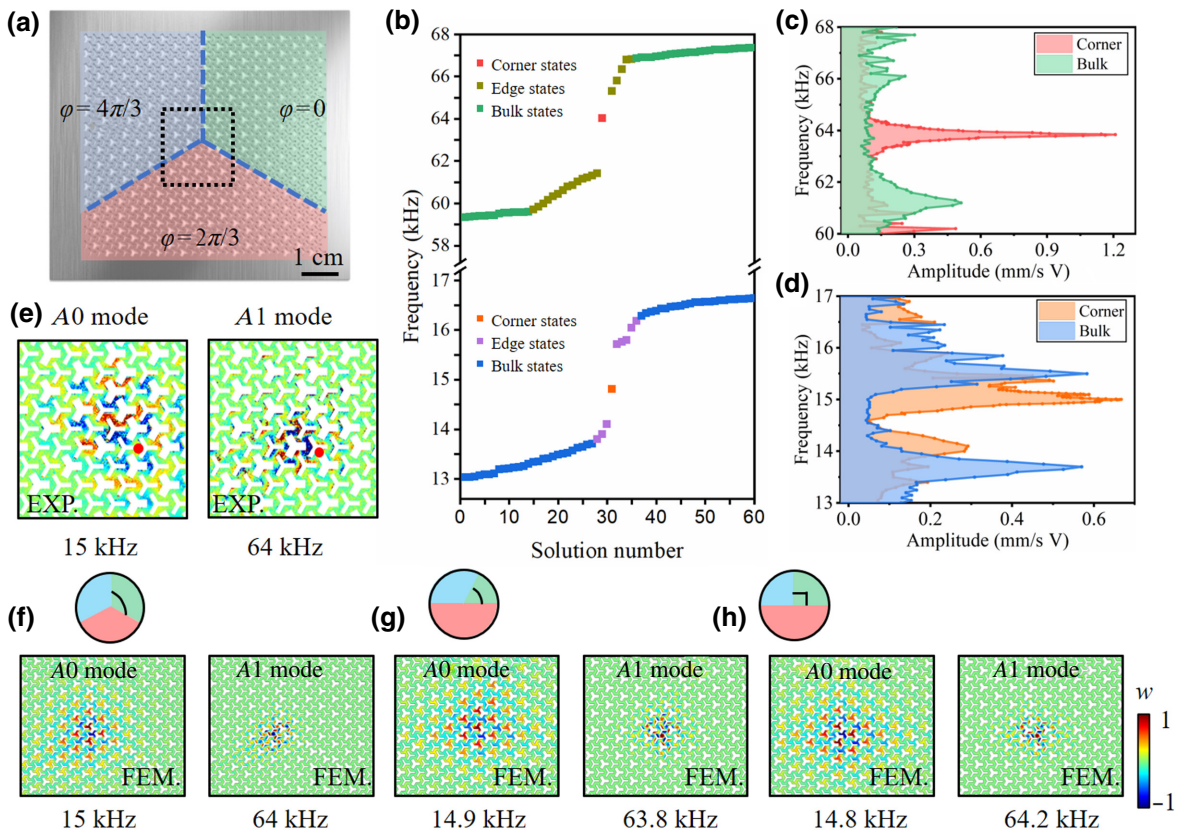


FIG. 6. Dual-band/mode discrete Dirac vortex states. (a) Schematic of discrete Dirac vortex formed by three realizations with angle differences of 120° (i.e., $\varphi = 0^\circ$, 120° , and 240°). (b) Numerically evaluated eigenfrequencies for sample A0 (low-frequency region) and A1 (high-frequency region) modes. The 2D bulk, 1D edge, and 0D corner states are marked. Measured mechanical energy density spectra near (c) A0 and (d) A1 corner states. (e) Measured mechanical displacement fields of A0 and A1 Dirac vortexes. (f) Calculated results for experimental sample. Calculated results for corner states in domains with angles of (g) 60° and (h) 90° .

Appendix G). Some edge states appear at the upper and lower extremes of the bulk band gap. Consequently, the “pure” band gap that allows the 0D corner states to exist is reduced, but within a tolerable range. In the QSH system, most mechanisms for corner state construction require strong modulation of the crystal symmetry [51,52]. In this manner, a band gap can be generated in the original continuous 1D edge states, thus yielding 0D corner states. However, our mechanism does not impose similar onerous requirements.

Figures 6(c) and 6(d) show the measured mechanical energy density spectra of the A0 and A1 corner states, respectively. Peaks appear in both the A0 and A1 bulk band gaps, verifying the existence of discrete vortex localizations of dual bands/modes. The frequencies of the two corner states are experimentally measured as 15 and 60 kHz, respectively, which correspond well with the calculation-based expectations. We further experimentally map the mechanical field distributions of the A0 and A1 Dirac vortex states, as shown in Fig. 6(e). Comparison of these distributions reveals that the A1 vortex state has a significantly smaller mode volume than that of A0; this result is

similar to the findings for their 1D edge states shown in Fig. 5. Figure 6(f) shows the results of the numerical simulation; the experiments and simulations correspond well. Importantly, the method adopted in this study can easily realize topological 0D corner states constructed from various domains of discrete angles. Figures 6(g) and 6(h) show the corner states constructed for domain angles of 60° and 90° , respectively. The difference between them is limited to a frequency offset. Other angles can also be used (see Fig. 15, Appendix H for more details). Therefore, the TCSs can be realized in various geometric structures through discrete Dirac vortices from aperiodic Kekulé modulations. Moreover, we can use phase modulation between more crystal domains to achieve the same Dirac vortex, or repeat the same domains to achieve a Dirac vortex with an n_w of 2 or higher; these characteristics yield considerably richer designability than those available for existing techniques.

VI. CONCLUSION

This study demonstrates a dual-band, dual-mode topological plate PnC for elastic waves in solids, which

constitute important media for information processing. In particular, dual-band equipment facilitates efficient and stable wireless networking. The low- and high-frequency operating bands of the proposed PnC are approximately 15 and 65 kHz, respectively, corresponding to the $A0$ and $A1$ Lamb modes, respectively. In experiments, we verify that the PnC supported dual-band 1D helical edge states and 0D Dirac vortexes of high quality; the approach to the latter is more convenient and diverse than traditional designs, owing to use of discrete Kekulé modulation. Experiments reveal that the high-frequency $A1$ modes have superior skin depth during transmission than the low-frequency $A0$ modes and, thus, the 0D resonance based on the former has higher quality and smaller mode volume. However, the $A1$ mode exhibits significantly greater loss than the $A0$ mode. The proposed dual-mode topology material exhibits clearly separated working bands, with a total bandwidth exceeding 20% without optimization. Through band engineering (e.g., to increase δW or for topology optimization), the available bandwidth is expected to reach 35% or higher [53]. In addition, the simple structure of our proposed PnC endows it with high scalability.

With current mainstream micro-nano processing technology, the operating frequency of the proposed PnC can easily reach values in the megahertz and gigahertz ranges. In addition, although nonpiezoelectric materials are employed for verification in our experiment, the PnC can be extended to the piezoelectric materials commonly used in integrated microwave acoustic devices (such as thin-film lithium niobate, lithium tantalate, and aluminum nitride), for direct assembly into a monolithic integrated phononic chip [54,55]. Moreover, the dual-band design is not only suitable for the A modes, but also for the S , SH, and higher-order modes [56]. This work is expected to promote and proliferate solid-state topology PnCs, and aid the development of future topological-phononic integrated circuits with multifunctionality, large bandwidth, and antijamming capabilities.

ACKNOWLEDGMENTS

The work was jointly supported by the National Key R&D Program of China (Grant Nos. 2021YFB3801801, 2017YFA0305100 and 2017YFA0303702) and the National Natural Science Foundation of China (Grant Nos. 11890702, 92163133, and 51732006). We also acknowledge the support of the Natural Science Foundation of Jiangsu Province, and Fundamental Research Funds for Central Universities.

APPENDIX A: POLARIZATION INDEX P_z

We distinguished the out-of-plane and in-plane modes of mechanical waves based on their polarization indexes P_z ; these modes are labeled with different colors in Fig. 1(d). The out-of-plane components directly calculated using P_z

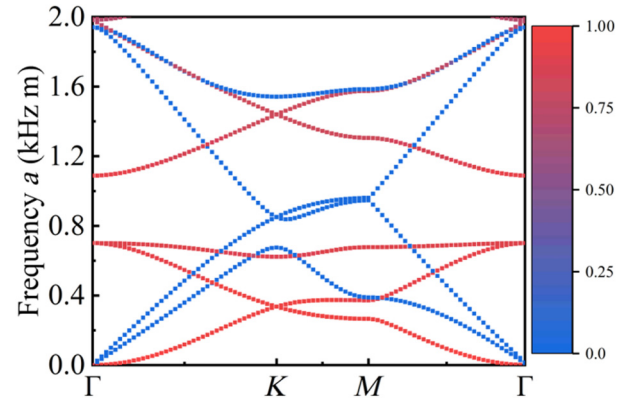


FIG. 7. Calculated mechanical band structure of plate PnC for arm widths $W_A = W_B = W_C$. The color map indicates the out-of-plane P_z values.

are shown in Fig. 7. For the in-plane extensional and SH modes, the P_z indexes are close to zero. For the out-of-plane flexural modes, the P_z indexes are close to 1. This result further confirms that the extensional and SH modes (both in-plane) of these PnCs are decoupled from their out-of-plane flexural modes, because they have mirror symmetry on the PnC plate plane.

APPENDIX B: BAND FOLDING

Figure 8 shows the band-folding process. Figure 8(a) shows two types of BZ, i.e., for a primitive and an enlarged unit cell. Figure 8(b) shows that four-fold degeneracy appears at the point where the reduced (first) BZ is folded from two two-fold degeneracies at the K_I and K'_I points of the extended BZs.

APPENDIX C: MECHANICAL VIBRATIONS OF MODES NEAR BAND GAPS

Figure 9 shows mechanical vibrations of modes near band gaps under applied homogeneous Kekulé modulation with $\varphi = 0$ and π , respectively. Comparison of the modes near the band gap confirms that the two mechanical insulators (with $\varphi = 0$ and π) exhibit band inversion at both frequencies of the $A0$ and $A1$ modes.

APPENDIX D: BAND-GAP SIZE WITH RESPECT TO MODULATION STRENGTH δW

We study the relationship between the modulation strength δW and the band gaps; the results are shown in Figs. 10(a) and 10(b). As δW increases, both the $A0$ and $A1$ band gaps increase linearly.

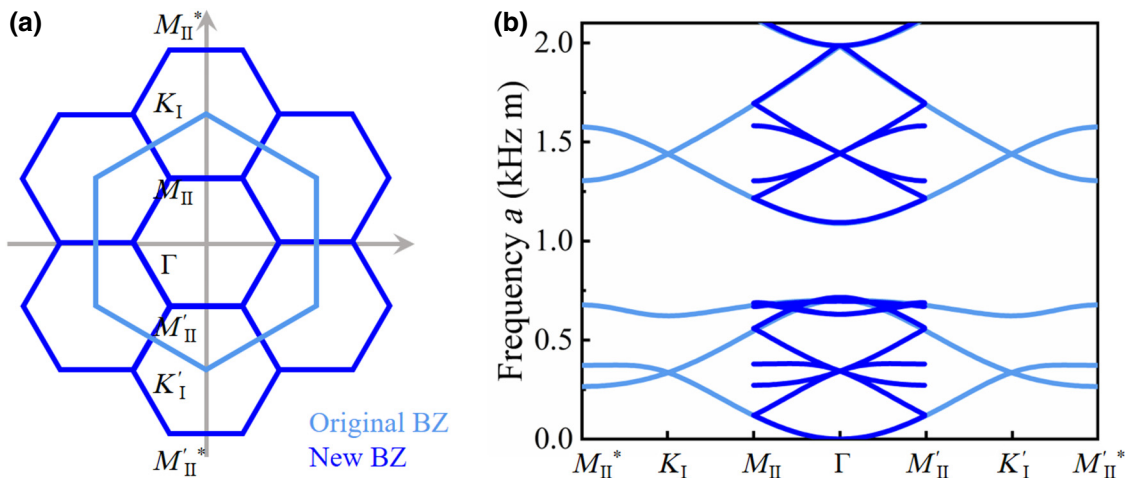


FIG. 8. Two choices of unit cell for the same PnC in the lattice. (a) Two types of BZ, i.e., for primitive and enlarged unit cell. (b) Band dispersions in extended BZs, in M_{II}^* , K_1' , M_{II}' , Γ , M_{II} , K_1 to M_{II}^* direction. They indicate nonphysical band folding, i.e., $\mathbf{G} + \mathbf{k}_0 \rightarrow \mathbf{k}_0$, from the extended BZs to the reduced (first) BZ.

APPENDIX E: EXPERIMENTALLY MEASURED PROJECTED ENERGY BANDS FOR A0 AND A1 LAMB MODES WITH TOPOLOGICAL INTERFACE

Experimentally measured projected energy bands for the $A0$ and $A1$ Lamb modes are shown in Figs. 11(a) and 11(b), respectively. Using the spatial Fourier transform method, we experimentally map the edge-state band structures. The measurement results match the theory-based expectations.

APPENDIX F: NUMERICAL CALCULATION OF TOPOLOGICALLY PROTECTED VHF AND UHF DUAL-BAND MONOLITHIC INTEGRATED ACOUSTIC TRANSMISSION LINES

In order to verify that the simple structure of our proposed PnC endows it with high scalability, we theoretically transfer a similar structure to a z -cut LiNbO₃ single-crystal film to see whether a dual-band topological protected transmission line can be achieved on microwave

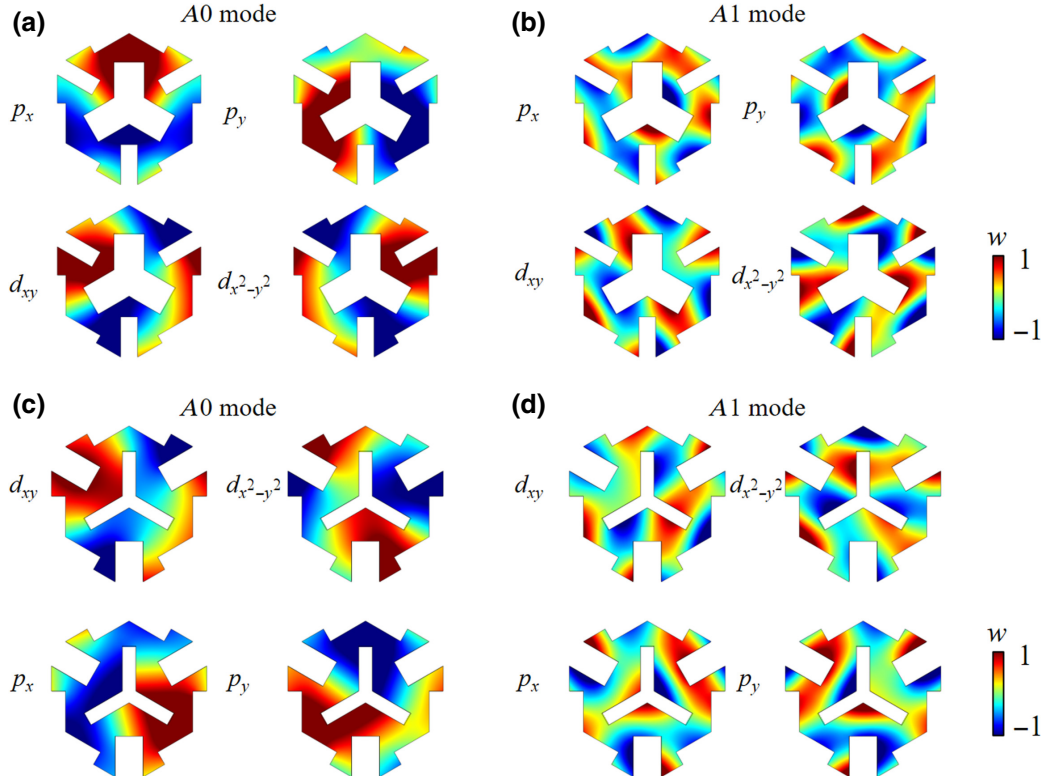


FIG. 9. (a)–(d) Mechanical vibrations of modes near band gaps, exhibiting four similar symmetries. Kekulé modulations with $\varphi = 0$ and π are adopted in (a),(b) and (c),(d), respectively. As they are analogous to atomic orbitals, we label these modes p_x , p_y , d_{xy} , and $d_{x^2-y^2}$. The colors indicate their displacement magnitudes.

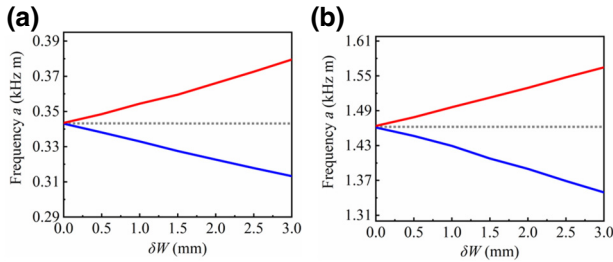


FIG. 10. Bandgap sizes for (a) $A0$ and (b) $A1$ Lamb waves with respect to δW .

frequencies. This PnC structure is shown in Fig. 12(a), using the same Z-shaped waveguide as in the main text, and placing interdigital transducers (IDTs) at both ends to realize the integration of the topologically protected transmission line and the microwave acoustic source/receiver. In numerical simulations, the thickness of z -cut LiNbO_3 is 800 nm, and the lattice period a is $3.695 \mu\text{m}$, as shown in Fig. 12(b). Figure 12(c) shows the elastic band structures under a homogeneous Kekulé modulation with $\varphi = 0$, which displays that there are also dual band gaps, one at vhf (approximately 110 MHz) and the other at uhf

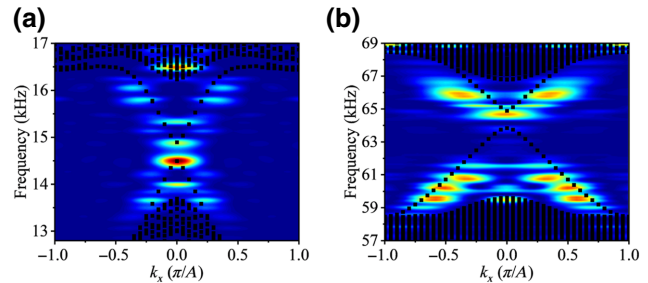


FIG. 11. Calculated (black dotted lines) and experimentally measured (blue and red regions) projected energy bands for (a) $A0$ and (b) $A1$ Lamb modes with topological interface.

(approximately 500 MHz). Therefore, elastic dual-band topological helical edge states can be constructed with calculation results shown in Fig. 12(d).

The difference between the microacoustic device and the macroaluminum plate in the main text is that the effect of the in-plane mode cannot be ignored. As shown in Fig. 12(c), in-plane modes (e.g., S and SH modes) exist in the topological band gap of the out-of-plane modes (e.g., A modes). In the main text, since only out-of-plane modes

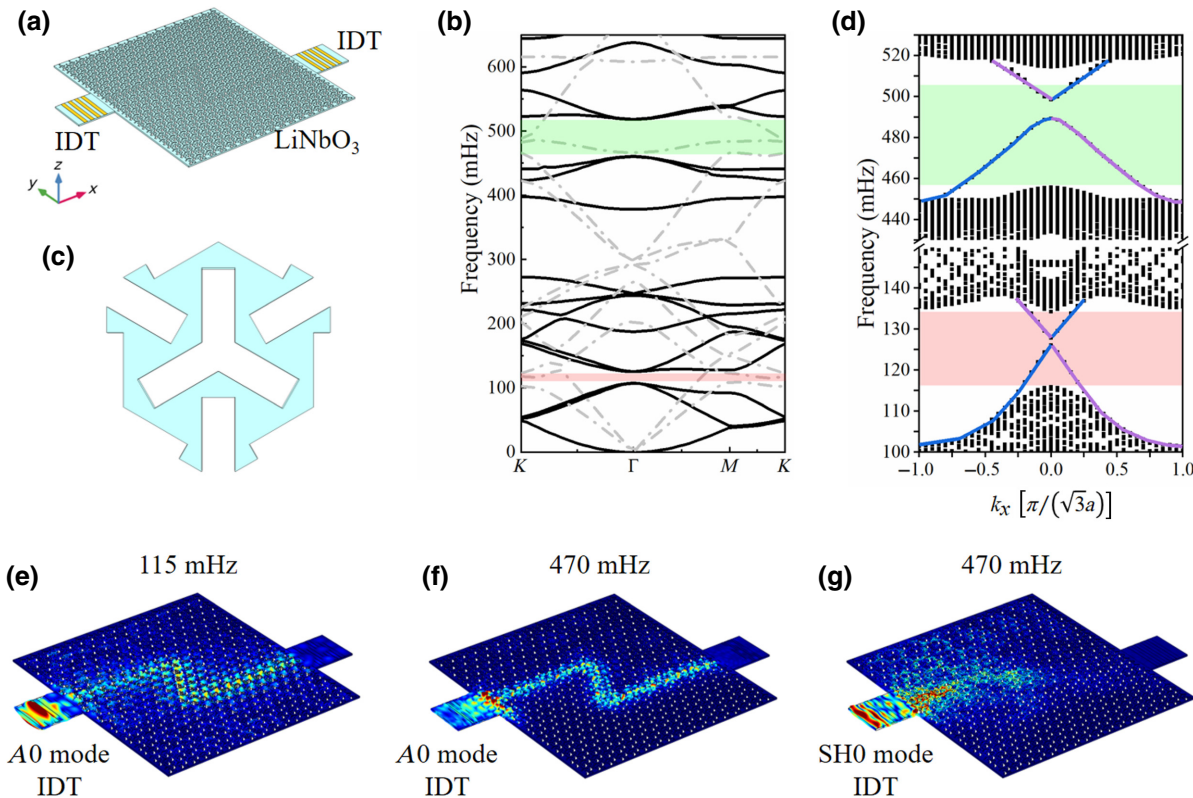


FIG. 12. Topologically protected vhf and uhf dual-band monolithic integrated acoustic transmission lines. (a) Schematic diagram of the device structure. (b) Schematic diagram of unit cell structure. (c) Elastic band structures under a homogeneous Kekulé modulation with $\varphi = 0$. (d) Calculated band structures for $A0$ and $A1$ modes in the interface between OI ($\varphi = 0$) and TI ($\varphi = \pi$). In (e) vhf and (f) uhf bands, $A0$ mode IDTs successfully excite the ($A0$ and $A1$) topological edge states at corresponding frequencies. (g) As a comparison, SH0 mode IDT cannot excite the ($A1$) topological edge states of the uhf.

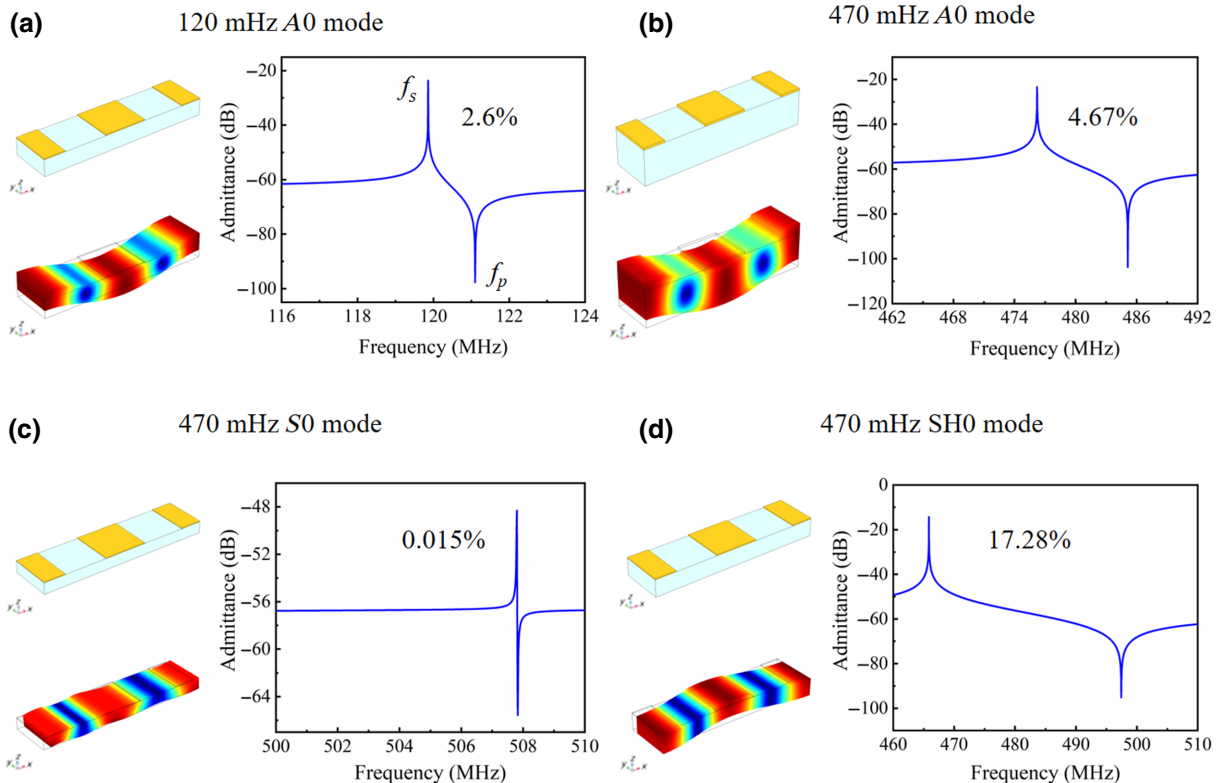


FIG. 13. A_0 , S_0 , and SH_0 mode IDTs. Geometric structures, vibration fields, and admittance spectra for the (a) 120-MHz A_0 mode, (b) 470-MHz A_0 mode, (c) 470-MHz S_0 mode, and (d) 470-MHz SH_0 mode IDTs. Their effective electromechanical coupling coefficients are calculated using the following formula: $k_{\text{eff}}^2 = (\pi^2/8)[(f_p^2 - f_s^2)/f_s^2]$.

can be measured experimentally using a laser vibrometer, we do not need to pay attention to the in-plane modes in the elastic band structure. In microacoustic devices, we have to set IDTs according to these in-plane and out-of-plane modes to excite the topological edge states of the target. As shown in Fig. 13, we design A_0 mode IDTs of 120 and 470 MHz to excite the corresponding edge states of the same frequencies. The vhf and uhf topological edge states are successfully excited using this A_0 mode IDT, as shown in Figs. 12(e) and 12(f).

It is further confirmed that the in-plane mode IDT cannot excite the out-of-plane mode edge state. In zx -cut LiNbO_3 film, since the S_0 mode IDT [see Fig. 13(c)] has a very small effective electromechanical coupling coefficient, we use the SH_0 mode IDT with an effective electromechanical coupling coefficient of over 17% [see Fig. 13(d)] for demonstration. As shown in Fig. 12(g), the SH_0 mode IDT cannot excite the edge state of the A modes.

Hence, the experimental study of the dual-band PnC on aluminum plate has an important guiding role in the future combination of topological physics/functions and integrated microwave acoustics. Theoretical and numerical calculations prove that as long as there is a topologically protected band gap for the in-plane or out-of-plane modes,

a monolithic integrated topological protected transmission line can be formed, i.e., there is no need to construct a full-mode band gap. With the rapid development of lithium niobate micro-nano processing technology, we believe that our proposed PnC will soon be implemented for frequencies of gigahertz and beyond.

APPENDIX G: CALCULATED PROJECTED ENERGY BANDS FOR A_0 AND A_1 LAMB MODES OBTAINED FOR DIFFERENT TOPOLOGICAL INTERFACES

We calculate the projected energy bands for A_0 and A_1 Lamb modes corresponding to different topological interfaces. In each case, the interface consists of two lattices randomly selected from three lattices with modulation phases of $\varphi = 0$, $2\pi/3$, and $4\pi/3$, as shown in Fig. 14. Because the entire PnC has C_{3v} symmetry, the projected energy bands of the different interfaces are the same.

APPENDIX H: DISCRETE DIRAC VORTEX STATES WITH DIFFERENT STRUCTURES

The discrete Dirac vortex states reported in this study are formed by three crystal domains with $\varphi = 0$, $2\pi/3$, and

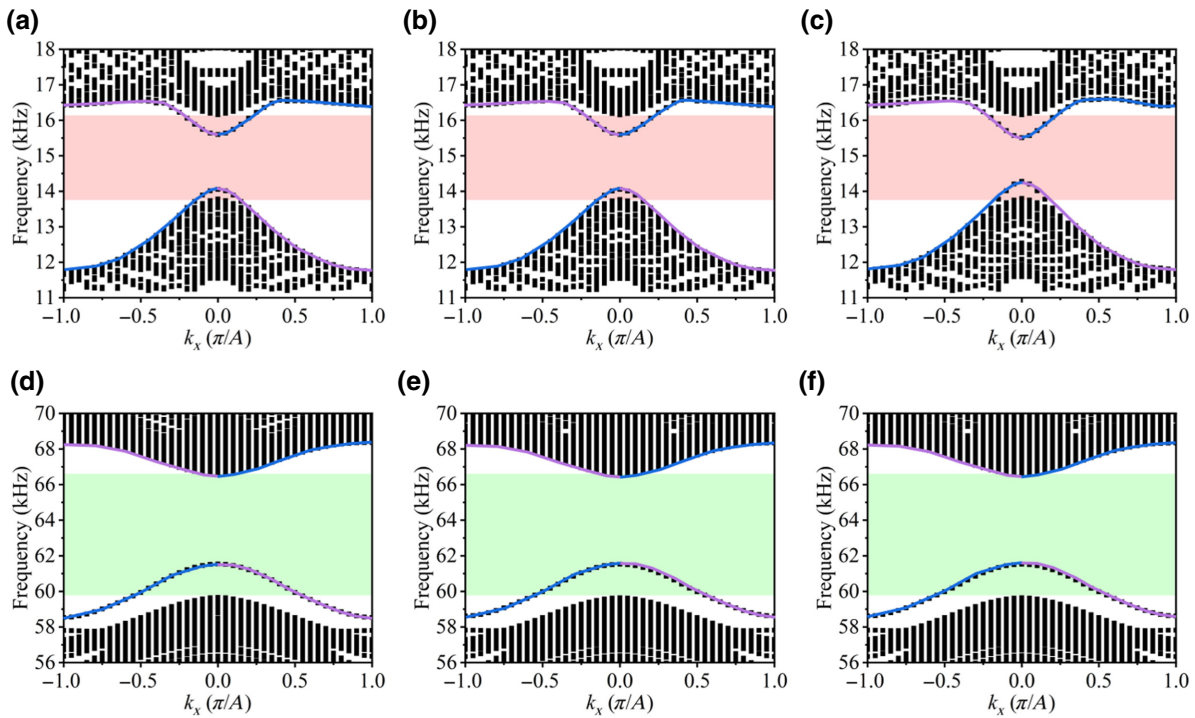


FIG. 14. Calculated projected energy bands for A0 and A1 Lamb modes obtained for different topological interfaces created using two lattices selected from lattices with $\varphi = 0, 2\pi/3$, or $4\pi/3$. Results for topological interfaces between lattices with (a) $\varphi = 0$ and (d) $\varphi = 2\pi/3$, (b) $\varphi = 0$ and (e) $\varphi = 4\pi/3$, and (c) $\varphi = 2\pi/3$ and (f) $\varphi = 4\pi/3$.

$4\pi/3$. Hence, we obtain a single vortex with the simplest winding number (i.e., $n_w = 1$), as shown in Fig. 15(a). Discrete Dirac vortex states can also be formed using more crystal domains, as shown in Figs. 15(b) and 15(c), with different φ . Moreover, we can repeat the same domains to achieve a Dirac vortex with $n_w \geq 2$.

APPENDIX I: SAMPLE FABRICATION AND EXPERIMENTAL MEASUREMENT PROCEDURE

A 5052-model aluminum plate is used to prepare the PnC plate. The PnC structure is processed on an aluminum plate using laser cutting. A 2-inch margin on the boundary

of the plate is left untreated for application of 3MTM Damping Foil 2552, which is used to reduce unwanted wave reflection from the edges during the test. Ultrasonic transducers with center frequencies of 15 and 65 kHz, which are bonded with an acrylic structural adhesive, are used as actuators. The signal from the signal generator (Tektronix AFG3252C) is amplified by a power amplifier (Falco Systems WMA-300) to excite the transducer. A scanning laser Doppler vibrometer system (Sunny Instruments Singapore, LV-S01) is used to test the out-of-plane vibration signals of the elastic waves. The laser vibrometer signal is finally recorded by a National Instruments acquisition card.

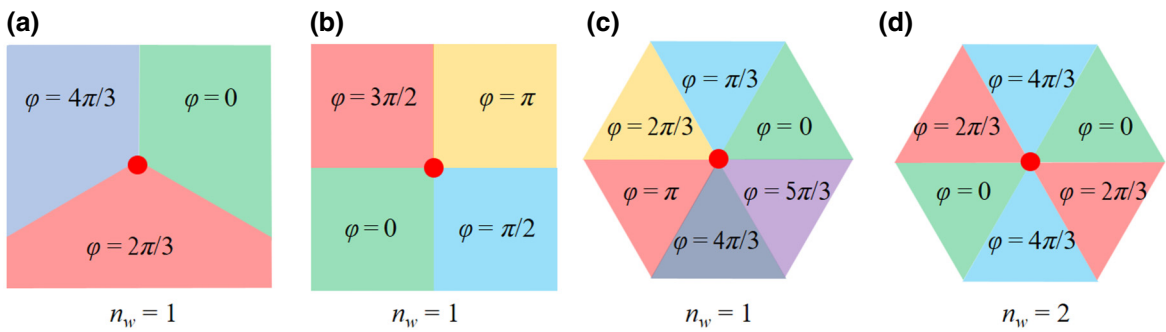


FIG. 15. Discrete Dirac vortex states with (a) three, (b) four, and (c) six realizations and $n_w = 1$. (d) Vortex with $n_w = 2$.

- [1] M. Naser-Moghadasi, R. Sadeghzadeh, L. Asadpor, and B. S. Virdee, A small dual-band CPW-fed monopole antenna for GSM and WLAN applications, *IEEE Antennas Wirel. Propag. Lett.* **12**, 508 (2013).
- [2] J. Chen, K. F. Tong, A. Al-Armaghany, and J. Wang, A dual-band dual-polarization slot patch antenna for GPS and Wi-Fi applications, *IEEE Antennas Wirel. Propag. Lett.* **15**, 406 (2015).
- [3] R. Weigel, D. P. Morgan, J. M. Owens, A. Ballato, K. M. Lakin, K. Y. Hashimoto, and C. C. Ruppel, Microwave acoustic materials, devices, and applications, *IEEE Trans. Microw. Theory Tech.* **50**, 738 (2002).
- [4] S. Gong, R. Lu, Y. Yang, L. Gao, and A. E. Hassanien, Microwave acoustic materials, devices, and applications, *IEEE J. Microw.* **1**, 601 (2021).
- [5] Z. Wang, Y. Chong, J. D. Joannopoulos, and M. Soljacic, Observation of unidirectional backscattering-immune topological electromagnetic states, *Nature* **461**, 772 (2009).
- [6] L. H. Wu and X. Hu, Scheme for Achieving a Topological Photonic Crystal by Using Dielectric Material, *Phys. Rev. Lett.* **114**, 223901 (2015).
- [7] X. Cheng, C. Jouvaud, X. Ni, S. H. Mousavi, A. Z. Genack, and A. B. Khanikaev, Robust reconfigurable electromagnetic pathways within a photonic topological insulator, *Nat. Mater.* **15**, 542 (2016).
- [8] C. He, X. Ni, H. Ge, X. C. Sun, Y. B. Chen, M. H. Lu, X. P. Liu, and Y. F. Chen, Acoustic topological insulator and robust one-way sound transport, *Nat. Phys.* **12**, 1124 (2016).
- [9] S. Barik, A. Karasahin, C. Flower, T. Cai, H. Miyake, W. DeGottardi, M. Hafezi, and E. Waks, A topological quantum optics interface, *Science* **359**, 666 (2018).
- [10] S. H. Mousavi, A. B. Khanikaev, and Z. Wang, Topologically protected elastic waves in phononic metamaterials, *Nat. Commun.* **6**, 8682 (2015).
- [11] J. Vila, R. K. Pal, and M. Ruzzene, Observation of topological valley modes in an elastic hexagonal lattice, *Phys. Rev. B* **96**, 134307 (2017).
- [12] C. Brendel, V. Peano, O. Painter, and F. Marquardt, Snowflake phononic topological insulator at the nanoscale, *Phys. Rev. B* **97**, 020102 (2018).
- [13] S. Y. Yu, C. He, Z. Wang, F. K. Liu, X. C. Sun, Z. Li, H. Z. Lu, M. H. Lu, and Y. F. Chen, Elastic pseudospin transport for integrable topological phononic circuits, *Nat. Commun.* **9**, 3072 (2018).
- [14] M. Miniaci, P. K. Pal, B. Morvan, and M. Ruzzene, Experimental Observation of Topologically Protected helical Edge Modes in Patterned Elastic Plates, *Phys. Rev. X* **8**, 031074 (2018).
- [15] J. Cha, K. W. Kim, and C. Daraio, Experimental realization of on-chip topological nano-electromechanical metamaterials, *Nature* **564**, 229 (2018).
- [16] M. Yan, J. Lu, F. Li, W. Deng, X. Huang, J. Ma, and Z. Liu, On-chip valley topological materials for elastic wave manipulation, *Nat. Mater.* **17**, 993 (2018).
- [17] R. Chaunsali, C. W. Chen, and J. Yang, Experimental demonstration of topological waveguiding in elastic plates with local resonators, *New J. Phys.* **20**, 113036 (2018).
- [18] T. W. Liu and F. Semperlotti, Synthetic kramers pair in phononic elastic plates and helical edge states on a dislocation interface, *Adv. Mater.* **33**, 2005160 (2021).
- [19] Z. D. Zhang, C. Cheng, S. Y. Yu, M. H. Lu, and Y. F. Chen, Electrically Tunable Elastic Topological Insulators Using Atomically Thin Two-Dimensional Materials Pinned on Patterned Substrates, *Phys. Rev. Appl.* **15**, 034015 (2021).
- [20] J. Chen, H. Huang, S. Huo, Z. Tan, X. Xie, J. Cheng, and G. L. Huang, Self-ordering induces multiple topological transitions for in-plane bulk waves in solid phononic crystals, *Phys. Rev. B* **98**, 014302 (2018).
- [21] M. Serra-Garcia, V. Peri, R. Süsstrunk, O. R. Bilal, T. Larsen, L. G. Villanueva, and S. D. Huber, Observation of a phononic quadrupole topological insulator, *Nature* **555**, 342 (2018).
- [22] H. Fan, B. Xia, L. Tong, S. Zheng, and D. Yu, Elastic Higher-Order Topological Insulator with Topologically Protected Corner States, *Phys. Rev. Lett.* **122**, 204301 (2019).
- [23] Q. Wu, H. Chen, X. Li, and G. Huang, In-plane Second-Order Topologically Protected States in Elastic Kagome Lattices, *Phys. Rev. Appl.* **14**, 014084 (2020).
- [24] Y. Wu, M. Yan, Z. K. Lin, H. X. Wang, F. Li, and J. H. Jiang, On-chip higher-order topological micromechanical metamaterials, *Sci. Bull.* **66**, 1959 (2021).
- [25] Q. Chen, L. Zhang, M. He, Z. Wang, X. Lin, F. Gao, Y. Yang, B. Zhang, and H. Chen, Valley-Hall photonic topological insulators with dual-band kink states, *Adv. Opt. Mater.* **7**, 1900036 (2019).
- [26] X. Zhang, Z. K. Lin, H. X. Wang, Z. Xiong, Y. Tian, M. H. Lu, Y. F. Chen, and J. H. Jiang, Symmetry-protected hierarchy of anomalous multipole topological band gaps in nonsymmorphic metacrystals, *Nat. Commun.* **11**, 65 (2020).
- [27] D. Jia, Y. Ge, H. Xue, S. Q. Yuan, H. X. Sun, Y. Yang, X. Liu, and B. Zhang, Topological refraction in dual-band valley sonic crystals, *Phys. Rev. B* **103**, 144309 (2021).
- [28] J. Ma, X. Xi, and X. Sun, Experimental demonstration of dual-band nano-electromechanical valley-Hall topological metamaterials, *Adv. Mater.* **33**, 2006521 (2021).
- [29] Z. Zhang, H. Long, C. Liu, C. Shao, Y. Cheng, X. Liu, and J. Christensen, Deep-Subwavelength holey acoustic second-order topological insulators, *Adv. Mater.* **31**, 1904682 (2019).
- [30] G. J. Tang, X. D. Chen, F. L. Shi, J. W. Liu, M. Chen, and J. W. Dong, Frequency range dependent topological phases and photonic detouring in valley photonic crystals, *Phys. Rev. B* **102**, 174202 (2020).
- [31] K. H. Kim and K. K. Om, Multiband photonic topological valley-Hall edge modes and second-order corner states in square lattices, *Adv. Opt. Mater.* **9**, 2001865 (2021).
- [32] Y. Chen, F. Meng, Z. Lan, B. Jia, and X. Huang, Dual-Polarization Second-Order Photonic Topological Insulators, *Phys. Rev. Appl.* **15**, 034053 (2021).
- [33] D. Hatanaka, I. Mahboob, K. Onomitsu, and H. Yamaguchi, Phonon waveguides for electromechanical circuits, *Nat. Nanotechnol.* **9**, 520 (2014).
- [34] M. Sledzinska, B. Graczykowski, J. Maire, E. Chavez-Angel, C. M. Sotomayor-Torres, and F. Alzina, 2D phononic crystals: Progress and prospects in hypersound and thermal transport engineering, *Adv. Funct. Mater.* **30**, 1904434 (2020).

- [35] R. H. Olsson III and I. El-Kady, Microfabricated phononic crystal devices and applications, *Meas. Sci. Technol.* **20**, 012002 (2009).
- [36] C. W. Chen, N. Lera, R. Chaunsali, D. Torrent, J. V. Alvarez, J. Yang, P. San-Jose, and J. Christensen, Mechanical analogue of a majorana bound state, *Adv. Mater.* **31**, 1904386 (2019).
- [37] P. Gao, D. Torrent, F. Cervera, P. San-Jose, J. Sánchez-Dehesa, and J. Christensen, Majorana-Like Zero Modes in Kekulé Distorted Sonic Lattices, *Phys. Rev. Lett.* **123**, 196601 (2019).
- [38] X. Gao, L. Yang, H. Lin, L. Zhang, J. Li, F. Bo, Z. Wang, and L. Lu, Dirac-vortex topological cavities, *Nat. Nanotechnol.* **15**, 1012 (2020).
- [39] A. J. Menssen, J. Guan, D. Felce, M. J. Booth, and I. A. Walmsley, Photonic Topological Mode Bound to a Vortex, *Phys. Rev. Lett.* **125**, 117401 (2020).
- [40] J. Ma, X. Xi, Y. Li, and X. Sun, Nanomechanical topological insulators with an auxiliary orbital degree of freedom, *Nat. Nanotechnol.* **16**, 576 (2021).
- [41] H. Lin and L. Lu, Dirac-vortex topological photonic crystal fibre, *Light Sci. Appl.* **9**, 202 (2020).
- [42] X. Wu, Y. Meng, Y. Hao, R. Y. Zhang, J. Li, and X. Zhang, Topological Corner Modes Induced by Dirac Vortices in Arbitrary Geometry, *Phys. Rev. Lett.* **126**, 226802 (2021).
- [43] S. Mittal, V. V. Orre, G. Zhu, M. A. Gorlach, A. Poddubny, and M. Hafezi, Photonic quadrupole topological phases, *Nat. Photonics* **13**, 692 (2019).
- [44] C. W. Peterson, W. A. Benalcazar, T. L. Hughes, and G. A. Bahl, Quantized microwave quadrupole insulator with topologically protected corner states, *Nature* **555**, 346 (2018).
- [45] X. Zhang, H. X. Wang, Z. K. Lin, Y. Tian, B. Xie, M. H. Lu, Y. F. Chen, and J. H. Jiang, Second-order topology and multidimensional topological transitions in sonic crystals, *Nat. Phys.* **15**, 582 (2019).
- [46] B. Y. Xie, G. X. Su, H. F. Wang, H. Su, X. P. Shen, P. Zhan, M. H. Lu, Z. L. Wang, and Y. F. Chen, Visualization of Higher-Order Topological Insulating Phases in two-Dimensional Dielectric Photonic Crystals, *Phys. Rev. Lett.* **122**, 233903 (2019).
- [47] X. Ni, M. Weiner, A. Alu, and A. B. Khanikaev, Observation of higher-order topological acoustic states protected by generalized chiral symmetry, *Nat. Mater.* **18**, 113 (2019).
- [48] H. Xue, Y. Yang, F. Gao, Y. Chong, and B. Zhang, Acoustic higher-order topological insulator on a kagome lattice, *Nat. Mater.* **18**, 108 (2019).
- [49] T. Kawarabayashi, Y. Inoue, R. Itagaki, Y. Hatsugai, and H. Aoki, Robust zero modes in disordered two-dimensional honeycomb lattice with Kekulé bond ordering, *Ann. Phys.* **435**, 168440 (2021).
- [50] R. Jackiw and P. Rossi, Zero modes of the vortex-fermion system, *Nucl. Phys. B* **190**, 681 (1981).
- [51] B. Xie, G. Su, H. F. Wang, F. Liu, L. Hu, S. Y. Yu, P. Zhan, M. H. Lu, Z. L. Wang, and Y. F. Chen, Higher-order quantum spin Hall effect in a photonic crystal, *Nat. Commun.* **11**, 3768 (2020).
- [52] C. W. Chen, R. Chaunsali, J. Christensen, G. Theocharis, and J. Yang, Corner states in a second-order mechanical topological insulator, *Commun. Mater.* **2**, 62 (2021).
- [53] R. E. Christiansen, F. Wang, and O. Sigmund, Topological Insulators by Topology Optimization, *Phys. Rev. Lett.* **122**, 234502 (2019).
- [54] Z. D. Zhang, S. Y. Yu, H. Ge, J. Q. Wang, H. F. Wang, K. F. Liu, T. Wu, C. He, M. H. Lu, and Y. F. Chen, Topological Surface Acoustic Waves, *Phys. Rev. Appl.* **16**, 044008 (2021).
- [55] K. C. Balram, M. I. Davanço, J. D. Song, and K. Srinivasan, Coherent coupling between radiofrequency, optical and acoustic waves in piezo-optomechanical circuits, *Nat. Photonics* **10**, 346 (2016).
- [56] R. Lu, T. Manzaneque, Y. Yang, and S. Gong, Lithium niobate phononic crystals for tailoring performance of RF laterally vibrating devices, *IEEE Trans. Ultrason. Ferroelectr. Freq. Control* **65**, 934 (2018).